Mechanical characterisation of tungsten–1 wt.% yttrium oxide as a function of temperature and atmosphere

T. Palacios , A. Jiménez , A. Muñóz , M.A. Monge , C. Ballesteros , J.Y. Pastor

A B S T R A C T

This study evaluates the mechanical behaviour of an Y_2O_3-dispersed tungsten (W) alloy and compares it to a pure W reference material. Both materials were processed via mechanical alloying (MA) and subsequent hot isostatic pressing (HIP). We performed non-standard three-point bending (TPB) tests in both an oxidising atmosphere and vacuum across a temperature range from 77 K, obtained via immersion in liquid nitrogen, to 1473 K to determine the mechanical strength, yield strength and fracture toughness. This research aims to evaluate how the mechanical behaviour of the alloy is affected by oxides formed within the material at high temperatures, primarily from 873 K, when the materials undergo a massive thermal degradation. The results indicate that the alloy is brittle to a high temperature (1473 K) under both atmospheres and that the mechanical properties degrade significantly above 873 K.

We also used Vickers microhardness tests and the dynamic modulus by impulse excitation technique (IET) to determine the elastic modulus at room temperature. Moreover, we performed nanoindentation tests to determine the effect of size on the hardness and elastic modulus; however, no significant differences were found. Additionally, we calculated the relative density of the samples to assess the porosity of the alloy.

Finally, we analysed the microstructure and fracture surfaces of the tested materials via field emission scanning electron microscopy (FE-SEM) and transmission electron microscopy (TEM). In this way, the relationship between the macroscopic mechanical properties and micromechanisms of failure could be determined based on the temperature and oxides formed.

1. Introduction

One major challenge in creating fusion reactors is developing the first wall materials, which are exposed to strong high-energy neutron fluxes (14 MeV). W and W alloys have recently been the focus of considerable attention because these materials were selected to manufacture several components within future fusion reactors. In particular, W and W alloys could be used as armour for the helium-cooled first wall in the demonstration fusion reactor (DEMO) designs and the helium-cooled divertor baffle area [1–4]. Pure tungsten is a suitable plasma-facing material because it has the highest melting point of any metal, good thermal conductivity, low tritium retention, low physical sputtering yield, high thermal resistance and high temperature strength. In the divertor, the material also has a structural function; therefore, a certain ductility is required within the operating temperature range [5]. However, W has a high ductile–brittle transition temperature (DBTT), ranging from 473 to 673 K using the same production route [6], and its recrystallisation temperature (RT) is too low, approximately 1500 K. These two temperatures define the operational temperature range for W.

Because recrystallisation and irradiation can embrittle W [7], it should contain dispersed oxide nanoparticles such as Y_2O_3, La_2O_3, CeO_2, ThO_2 or HfO_2. These nanoparticles not only enhance the recrystallisation temperature [8] but also prevent grain growth and stabilise the microstructure at high temperatures, which increases the high temperature strength and creep resistance. Furthermore, the large amount of grain boundaries in an ultrafine grain microstructure can serve as an effective sink for irradiation-induced point defects to improve the irradiation damage resistance [7]. In addition, nano-scaled grains can favour material ductility at lower temperatures. In recent years, we used a powder metallurgy route consisting of mechanical alloying (MA) and a subsequent sintering by hot isostatic pressing (HIP). This route efficiently produced oxide dispersion-strengthened (ODS) W alloys [9]. Moreover, the addition of Y_2O_3 was found to improve the mechanical properties of the W–Ti and W–V alloys, which was attributed to the good oxide dispersion and microstructure grain

Table 1
Starting powder properties.

Powder	Purity (%)	Average particle size (μm)
W	99.9	12
Y_2O_3	99.5	0.01–0.05

refinement [10]. Small angle neutron diffraction measurements and high resolution scanning electron microscopy (SEM) images indicate nanometric grain microstructures with finely dispersed oxide nanoparticles for the ODS W–1Y_2O_3 alloys [11].

2. Materials and samples

Pure W and a W–1 wt.% Y_2O_3 (W–1Y_2O_3) alloy were prepared by mixing the starting powders (Table 1) for 4 h. The powder mixtures then underwent MA inside a sealed WC vessel with a high-purity Ar atmosphere for 20 h in a high-energy planetary mill. We used WC balls with Ø 10 mm as the grinding media with a ball-powder ratio of 4:3. Afterwards, the alloyed powders were canned and degassed at 673 K for 24 h under vacuum before vacuum sealing. The starting, blended and alloyed powders were manipulated under a high-purity Ar atmosphere using a glove box.

A subsequent HIP at 1573 K for 2 h at a pressure of 195 MPa consolidated the canned powders. We then obtained cylinders with dimensions of 30 mm Ø and 50 mm in length cut by refrigerated electro-discharge machining to obtain bend bar specimens with nominal dimensions of $1.6 \times 1.6 \times 25$ mm^3.

We measured the oxygen content of the materials during the different fabrication steps by inert gas fusion infrared detection (LECO). For the pure W sample, the oxygen contents were 0.0662 wt.%, 0.533 wt.% and 0.312 wt.% before milling, after milling and after HIP, respectively. The oxygen contents of W–1Y_2O_3 after removing the contribution from O in Y_2O_3 were 0.047 wt.%, 0.369 wt.% and 0.282 wt.% before milling, after milling and after HIP, respectively.

3. Experimental methods

We measured the experimental density (ρ_{exp}) of the samples via Archimedes method using high purity ethanol at room temperature. Additionally, we calculated the theoretical density (ρ_{th}) using the density of each component and the following formula (1):

$$\rho_{th} = \frac{m_W + m_{Y_2O_3}}{m_W \rho_W^{-1} + m_{Y_2O_3} \rho_{Y_2O_3}^{-1}} \quad (1)$$

where m_x and ρ_x represent the mass ($m_W = 99$ g, $m_{Y_2O_3} = 1$ g) and density ($\rho_W = 19.25$ g/cm^3 and $\rho_{Y_2O_3} = 5.03$ g/cm^3), respectively, of the corresponding elements in the alloy.

Based on these two results (experimental and theoretical densities), we calculated the relative density (ρ_r) to determine the porosity of the materials.

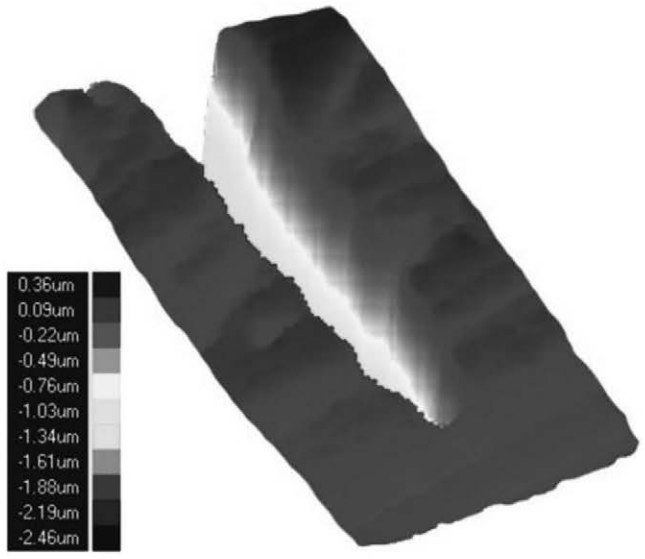

Fig. 2. Image of the notch tip radius based on profilometer.

Following ASTM Standard 384-89, we performed Vickers tests to measure the microhardness of the compacted materials. We used two loads (0.98 and 9.8 N) with an application time of 12 s to determine the influence of the applied load on the results. After removing the indenter from the surface, the lengths of the indentation diagonals were measured via optical microscopy.

We also performed nanoindentation tests using a NanoIndenter XP from the MTS Systems Corporation (Oak Ridge, TN, USA) equipped with a Berkovich tip. We calculated the material nanohardness from the obtained force–displacement curve using the Oliver and Pharr method [12]. These tests allowed both the nanohardness (nH) and elastic modulus (nE) to be obtained at room temperature. The results were comparable to those obtained via the Vickers tests for the hardness and IET method for the elastic modulus, which uses the natural vibration frequencies of the material [13]. To get an approximation of the theoretical elastic modulus, we used a model of maximum values [14], under the hypothesis of isodeformation:

$$E_{th} = E_W V_W + E_{Y_2O_3} V_{Y_2O_3} + E_{air} V_{air} \quad (2)$$

where E_x represent the elastic modulus ($E_W = 400$ GPa, $E_{Y_2O_3} = 177$ GPa, $E_{air} = 0$ GPa) and V_x the volumetric fraction of the corresponding elements in the alloy.

We performed a non-standard three-point bending (TPB) test on the smooth and laser-notched bend bars in air (oxidising atmosphere) for the temperature range between 77 K, obtained via liquid nitrogen immersion, and 1273 K and in vacuum (inert atmosphere) with a pressure of approximately 10^{-6} mbar and between 673 and 1473 K. Nevertheless, the major thermal degradation due to oxide evaporation began at 1073 K [15]. The bending fixture was

Fig. 1. Notch tip obtained in a fracture toughness sample using laser technology.

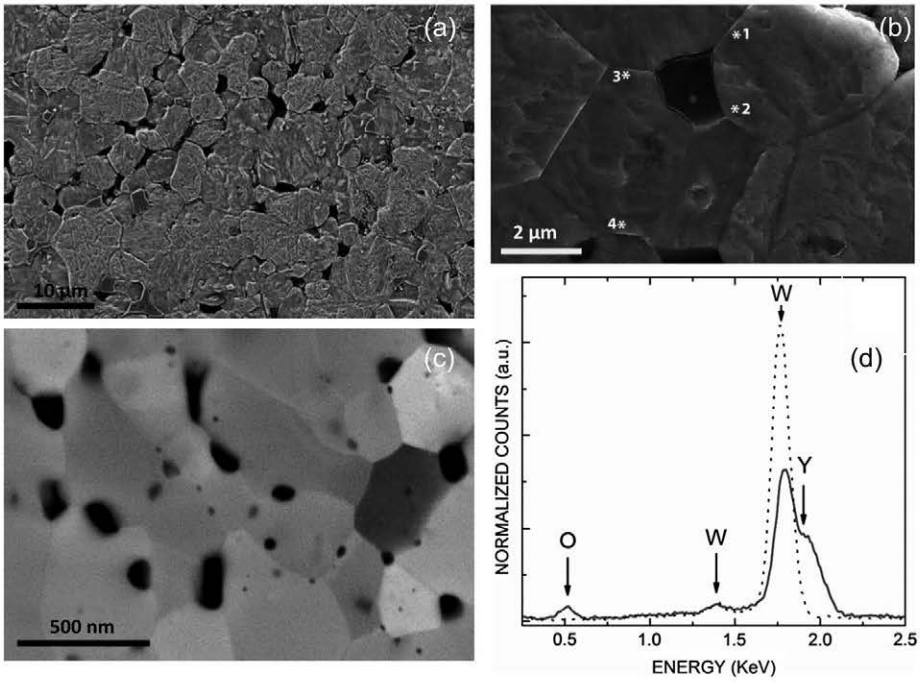

Fig. 3. (a) FE-SEM image showing the W–1Y_2O_3 alloy microstructure. (b) FE-SEM image showing the position from which the EDX spectral data were obtained. The composition calculated from the obtained EDX spectra corresponds to a W matrix with a Y content near 1.4 wt.% for spectrums 1 and 2 and near 0.5 wt.% for spectrums 3 and 4. (c) High magnification BSE-SEM image showing the W–1Y_2O_3 alloy microstructure. The black contrast regions at the grain boundaries correspond to W–Y–O complex oxides with an average Y content of 18%. (d) EDX spectra where the solid line corresponds to a representative EDX spectrum from the black areas, and the dotted line corresponds to the W-matrix. W (M-lines), Y (L-lines) and O (K-line) are marked by arrows.

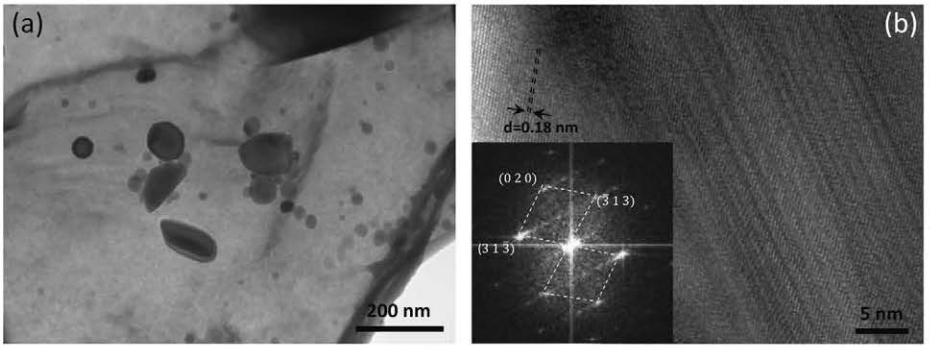

Fig. 4. (a) TEM image showing Y_2O_3 dispersed in the W matrix. (b) HR-TEM micrograph of an yttria nanoparticle. The insert shows the digital power spectra obtained for the micrograph, which indicates the yttria particles had a monoclinic crystal structure. The corresponding plane spacing of the indexed planes are $d_{020} = 0.18$ nm and $d_{313} = 0.21$ nm.

connected to an actuator and the testing machine frame using Al_2O_3 load bars. It was placed in a high-temperature furnace during the mechanical tests. We performed the TPB tests using displacement control with a rate of 100 µm/min. The load spans for the smooth and laser-notched bars were 16.0 and 8.5 mm, respectively. The heating rate was 30 K/min, and once we reached the set point, the heating was held for 10 min to thermally stabilise the system. We continuously monitored the load and load point displacement during the tests using a load cell and linear variable differential transformer induction transducer, respectively. We tested three to five samples for each material and at each temperature to ensure repeatability.

The force–displacement data obtained via the TPB tests and standard material strength formulas [16] provide σ–ε curves that can determine the maximum tensile bending strength at the fracture point. Because this method is restricted to the elastic bending regime, we used a 0.2% yield strength offset criteria in some cases that exhibit ductile behaviour at higher temperatures.

To calculate the appropriate fracture toughness values (K_{IC}), we measured the maximum load and initial notch length for each test via field emission scanning electron microscopy (FE-SEM) and used the appropriate formula [17]. We notched the fracture toughness samples using laser technology to obtain a notch tip near a crack (Figs. 1 and 2). We measured the notch length for all of the samples and obtained values of approximately 250 µm with tip radii between 5 and 20 nm.

We analysed the microstructure and fracture surfaces of the tested samples using FE-SEM. Additionally, we prepared thin 3 mm diameter foils for TEM analysis via a standard procedure that involves slicing and polishing. The final thinning was achieved in a TENUPOL 5 twin-jet polisher using 12.5% SO_4H_2 + 1.8% HF + 85.7% methanol as the electrolyte at 245 K. We performed the TEM

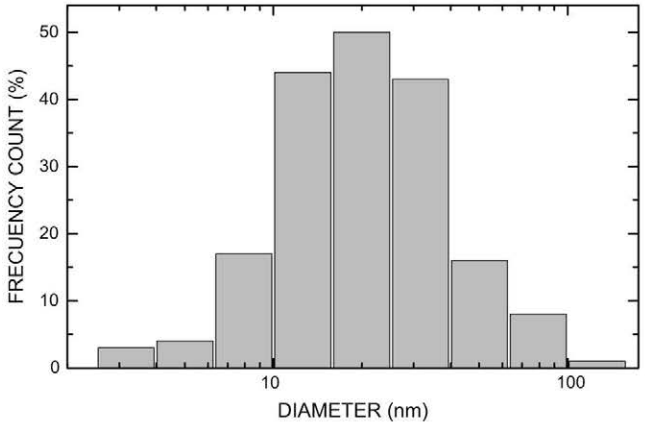

Fig. 5. Size distribution for the Y_2O_3 nanoparticles dispersed in the tungsten matrix.

Table 2
Experimental (ρ_{exp}) and theoretical (ρ_{th}) densities measured for the samples along with the relative density (ρ_r) calculated from them and the estimated porosity.

Material	ρ_{exp} (g/cm^3)	ρ_{th} (g/cm^3)	ρ_r (%)	Porosity (%)
Pure W	17.64 ± 0.02	19.25	91.64	8.36
W–1Y_2O_3	16.93 ± 0.02	18.72	90.44	9.56

Table 3
Elastic modulus measured via IET (E_{IET}), instrumented nanoindentation (nE) and theoretically calculated (E_{th}).

Material	E_{IET} (GPa)	nE (GPa)	E_{th} (GPa)
Pure W	338 ± 5	350 ± 40	400
W–1Y_2O_3	294 ± 1	310 ± 40	354

characterisation using a TECNAI 20-FEG equipped with an X-ray energy dispersive spectrometer (XEDS) operated at 200 kV with a scanning transmission electron microscopy (STEM) module, dark field high angle annular (HHADF) detector for Z-contrast imagining and X-ray energy dispersive spectrometer.

4. Results and discussion

4.1. Microstructure

The W–1Y_2O_3 alloy microstructure after the HIP is shown in Fig. 3(a). The HIP treatment grew Y-rich oxides at the grain boundary [18] as revealed by the black patches in the BSE-SEM electron images (Fig. 3(b) and (c)). Although the EDX–SEM analysis of the W–1Y_2O_3 revealed the presence of yttrium within the W grains (Fig. 3(b) and (c)), a differential concentration of Y_2O_3 could exist in these grains (Fig. 3(d)) because Y is not a completely solid solution in W and a dispersion of Y_2O_3 particles could occur.

The alloy microstructure exhibits a relatively well-mixed bimodal grain size morphology (Fig. 3(a)–(c)). This duplex grain size distribution consists of submicron and coarse grain populations, centred at ≈420 nm and ≈5.3 μm, respectively. Although some residual porosity was observed, it mainly occurred at triple junctions between the W grains (Fig. 3(a)).

The TEM observations provided more evidence of Y_2O_3 nanoparticles being dispersed within the W grains and detailed the nanoparticle morphology, size and crystal structure. The yttria particles dispersed in the W matrix were visible as spheroidal dispersoids of variable size; some of these particles formed via the

Table 4
Vickers microhardness (HV) for two different applied loads and the instrumented nanoindentation Berkovich hardness (nH).

Material	HV (GPa)		nH (GPa)
	9.8 N	0.98 N	0.6 N
Pure W	2.58 ± 0.03	3.4 ± 0.5	3.70 ± 0.09
W–1Y_2O_3	3.41 ± 0.02	3.73 ± 0.05	3.9 ± 0.7

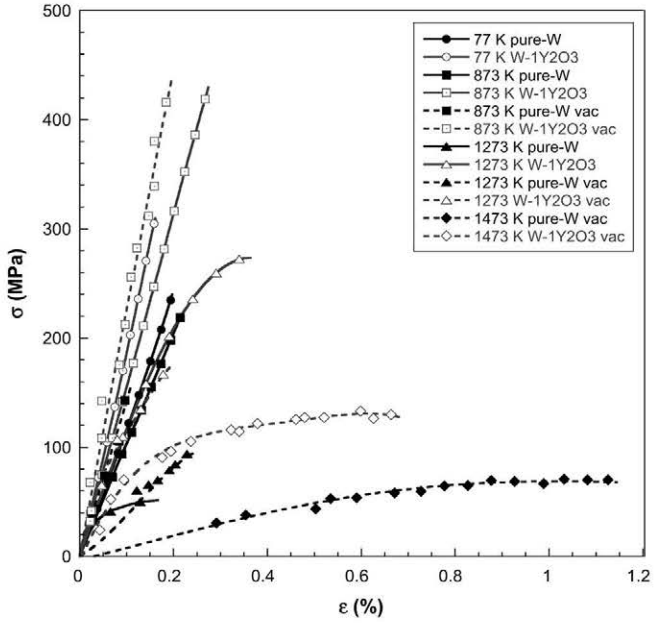

Fig. 6. Representative flexural σ–ε curves at different temperatures for pure W and W–1Y_2O_3. The unrepresented curves had similar linear elastic behaviour up to those one shown in the figure.

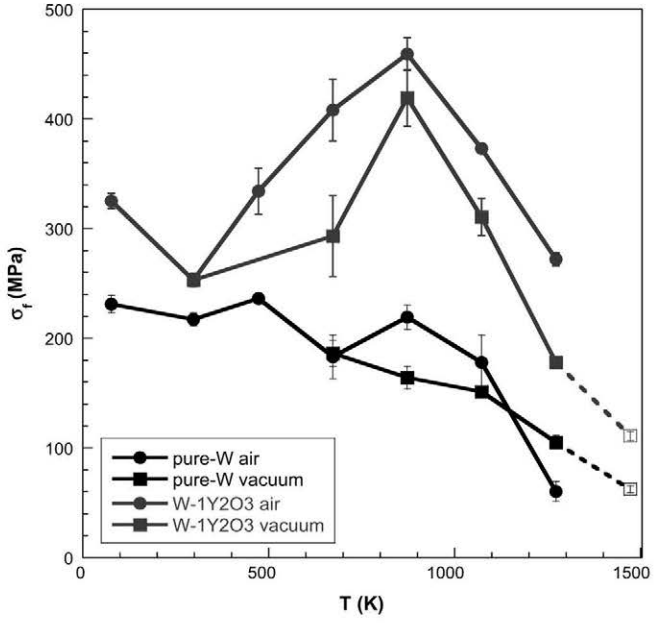

Fig. 7. Average flexural strength versus test temperature for the W–1Y_2O_3 alloy and pure W in air and under vacuum. The open symbols and dashed lines represent the yield strength at 0.2% when the materials exhibited a ductile behaviour.

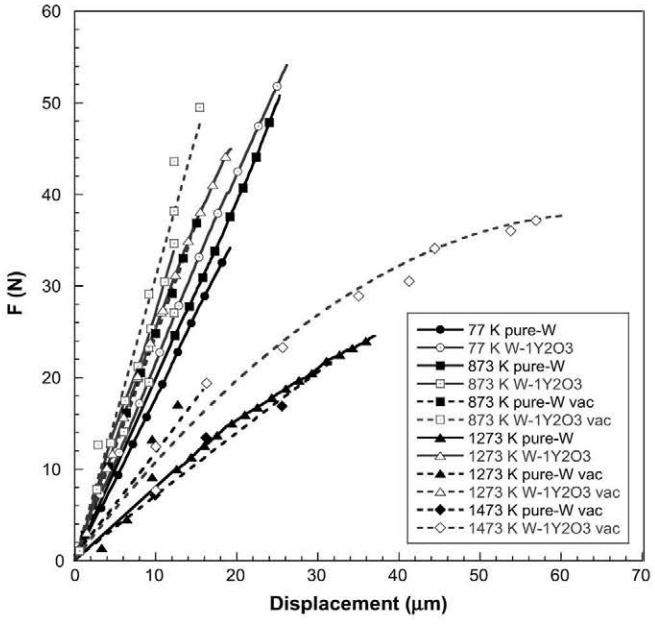

Fig. 8. Representative flexural force–displacement curves at different temperatures for notched samples of pure W and W–1Y_2O_3. The unrepresented curves had similar linear elastic behaviours to that shown in the figure until their failure.

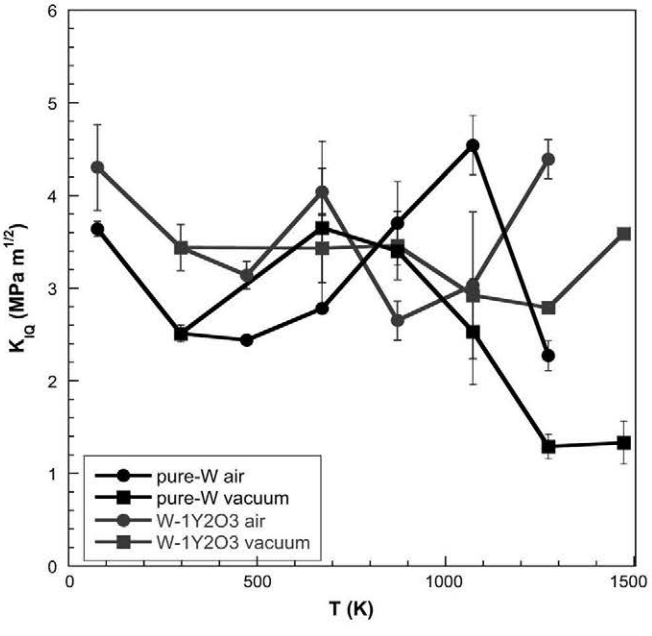

Fig. 9. Average fracture toughness versus test temperature for the W–1Y_2O_3 alloy and pure W in air and under vacuum.

agglomeration of several nanoparticles (Fig. 4(a)). The individual nanoparticles had a quasi-homogeneous size (the small, circular, light-grey particles in Fig. 4(a)). The nanoparticle chemistry was investigated via TEM using EDXS; in all the cases, the EDX spectra contained oxygen and were Y-rich.

The HRTEM characterisation showed no coherent nanoparticles within the matrix, which indicated that shearing the particles via dislocations may be difficult. Furthermore, we investigated the nanoparticle structure via electron diffraction pattern simulation using a fast Fourier transform (FFT) of the HRTEM images. The nanoparticle crystal structure was monoclinic with lattice parameters of $a = 13.91$ Å, $b = 3.49$ Å, $c = 8.612$ Å and $\beta = 100.12°$, which

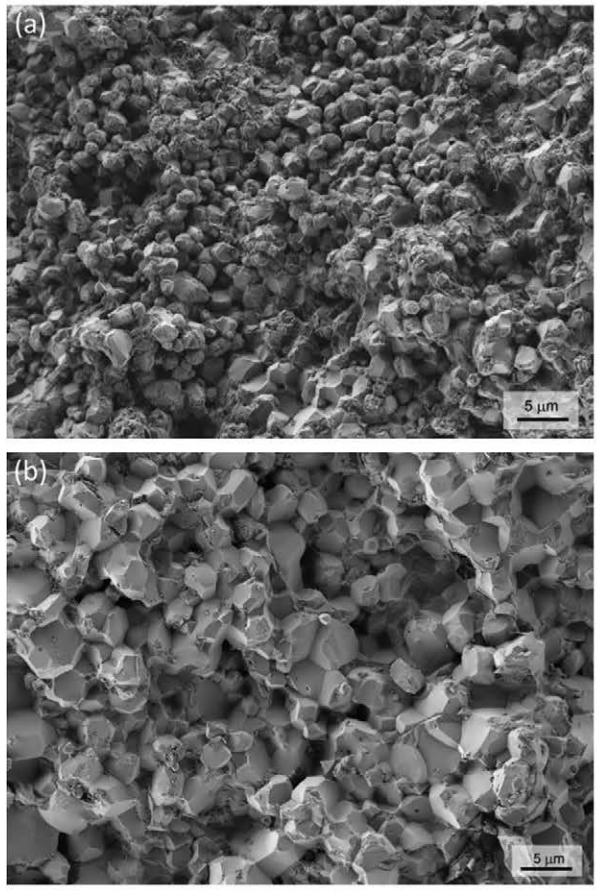

Fig. 10. Fracture surface of (a) pure W and (b) W–1Y_2O_3 tested at 300 K.

agrees well with Y_2O_3 nanoparticles (Fig. 4(b)). Moreover, numerous Y_2O_3 particles exhibited staking fault contrast fringes in the crystalline lattice (Fig. 4(b)). The formation of stacking fault defects in the Y_2O_3 monoclinic structures was commonly explained by the combination of strain and oxygen loss.

The particle size distribution of the spheroidal yttria particles obtained from the TEM images (Fig. 5) had a mode of 19.9 ± 1.0 nm in diameter that approximately corresponds to the starting Y_2O_3 nanopowder size. A detailed description of the pure W reference microstructure can be found in Ref. [19].

4.2. Mechanical properties and failure micromechanisms

The alloyed samples had lower densities than pure W (Table 2); therefore, their porosity had increased. More oxygen moved to the internal portion of the alloy due to this increased porosity. This porosity, as it was reported for some other materials [18], is not closed but is percolating, leading to the formation of interconnected channels that allow a homogeneous distribution of the oxygen. The small amount of 1 wt.% Y_2O_3 added, 3.72% in volume, is enough to stabilize the oxidation processes since, as it was previously reported, Y_2O_3 is very stable oxide with high melting point (around 2700 K) and an excellent chemical and thermal stability [20,21]. This addition allows to maintain or improve the mechanical properties of the alloy (Figs. 7 and 9).

The resultant elastic modulus (Table 3) indicated that adding Y_2O_3 significantly decreased the modulus, and the agreement between the different techniques was very good.

The Vickers microhardness test (Table 4) indicated the applied load had a small influence. Higher values were achieved using

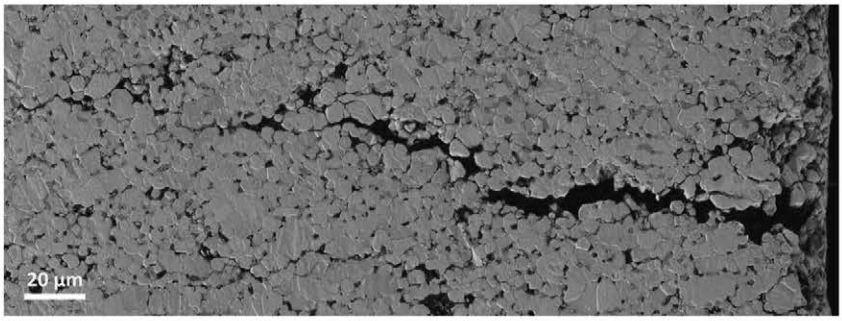

Fig. 11. Intergranular crack growth in the W–1Y_2O_3 alloy tested at 1473 K after a TPB test to determine its flexural strength.

the lower load, 0.98 N. These results are comparable to the instrumented nanoindented Berkovich tests (applied load of 0.6 N). There were no significant differences between these methods. In general, adding Y_2O_3 slightly increased the hardness value; however, all of the values were generally within the error of approximately 3.5 GPa.

The TPB test results for the flexural strength of both materials showed that the alloy behaviour was linearly elastic until fracture at almost all studied temperatures (Fig. 6). However, at 1473 K under vacuum, the samples exhibited a plastic deformation without breaking. In this case, the 0.2% yield strength offset was represented using open symbols and dashed lines (Fig. 7).

Adding Y_2O_3 increased the flexural strength across the entire temperature range where two intervals were distinguishable (Figs. 6 and 7):

- From 300 to 873 K. The alloy flexural strength increased to a maximum at 873 K in both atmospheres.
- From 873 to 1473 K. Above 873 K, the value decreased due to massive thermal degradation. At 1473 K, the properties had completely degraded even under a vacuum atmosphere, most likely due to the porosity decreasing the alloy cohesion. Despite this, the samples did not break, and a plastic behaviour was macroscopically observed with a crack between the grain boundaries (Fig. 11).

The DBTT was defined as when the σ–ε curves changed their behaviour from linearly elastic to plastic (Fig. 6). No improvement was observed upon the addition of Y_2O_3. For both materials, the DBTT was above 1273 K in vacuum. The high vacuum tests yielded reduced flexural strengths relative to those in air. This improvement of the values was attributed to the possible blunting of the surface defects due to superficial oxide formation. But at the same time, in air, there were a high temperature massive oxidation that completely degrades the properties.

The force–displacement curves obtained from the TPB tests involving the notched samples (Fig. 8) exhibited lineal elastic behaviour until their fracture for all studied temperatures. Adding Y_2O_3 to the alloy improved the behaviour at higher temperatures (Fig. 9) and reached a fracture toughness value of approximately 3–5 MPa $m^{1/2}$ while for the rest of the temperature range remained nearly constant. In comparison with literature data Veleva [18] reported analogous behaviour for W–1Y_2O_3 alloy processed also by HIP. This material was fully brittle from low to intermediate temperatures, with low fracture toughness values around 5.5 MPa $m^{1/2}$, and higher bending strength values at fracture in the range of 650–800 MPa. However, Battabyal [22] reported W–2Y_2O_3 alloys fabricated by pressing, sintering and hot forging with ductile tensile behaviour at 673–1273 K have weak Charpy impact properties at 773–1273 K.

For all of the temperatures studied, both the W–1Y_2O_3 alloy and pure W experienced a brittle fracture. The observed fracture surfaces were flat and showed a fracture decohesion at the grain boundary (Fig. 10).

As shown in the TPB test results, the primary benefit of adding Y_2O_3 is the increase in the values of flexural strength and fracture toughness of the alloy. This material inhibits oxide formation as shown by the test fracture surfaces at 1273 K in air (Fig. 12). We observe many differences between the fracture surfaces of these materials. The pure W surface (Fig. 12(a)) was completely covered with a yellowish dense oxide scale of WO_3. However, with the addition of 1 wt.% Y_2O_3 (Fig. 12(b)), the formation of this typical

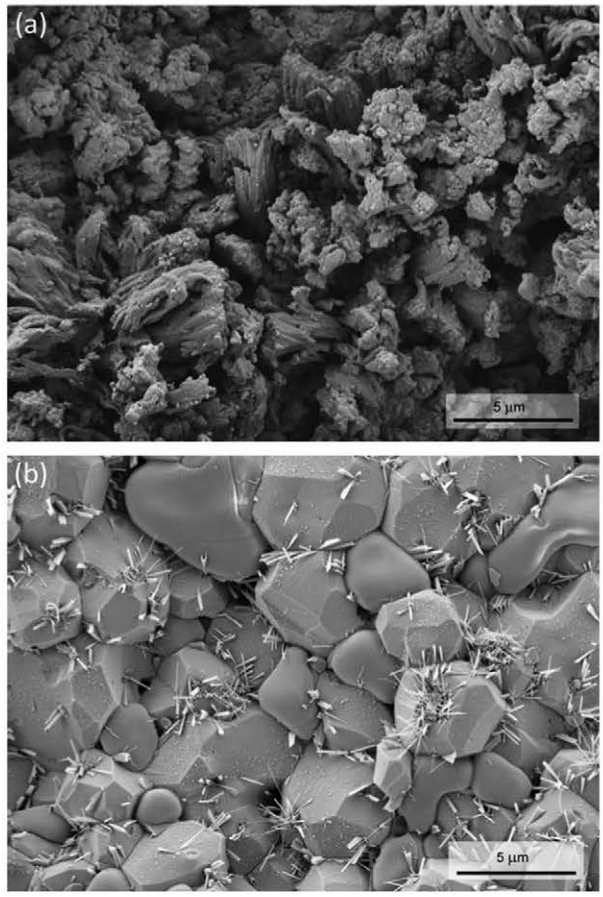

Fig. 12. Fracture surfaces of (a) pure W and (b) W–1Y_2O_3 tested at 1273 K in the oxidising atmosphere (air).

oxide scale is imperceptible at 1273 K. The W–1Y_2O_3 surface contains rounded grains rich in Y_2O_3 with oxide needles primarily concentrated around the polyhedral shapes (W grains). At this point, the linear oxidation kinetics of pure W observed over 1073 K [23] has probably changed in the alloy to a protective oxide scale with the dense oxide needles.

5. Conclusions

This study demonstrated the effects that high temperature had on the mechanical properties of a tungsten alloy containing dispersed Y_2O_3 nanoparticles in its matrix. The following conclusions were drawn from this study:

- After processing the alloy, the porosity increased and the elastic modulus decreased. Consequently, the hardness was improved and a slight load effect was observed.
- Adding Y_2O_3 to the tested alloy did not enhance the mechanical properties at lower temperatures; however, above 873 K where the oxidation processes becomes less intense, the Y_2O_3 alloy values were better than for pure W because Y_2O_3 further promotes the anti-oxidation efficacy of the material.
- In most cases, the vacuum tests yielded lower values than the air tests, which was most likely due to the superficial oxides blunting the defects and the notches tip radius.
- Fracture analysis of the tested samples showed a primarily intergranular breakage between the grain boundaries. This result supports the brittle behaviour observed during the tests.
- A bimodal grain morphology was observed. Polyhedral coarse W grains and rounded smaller grains containing dispersed yttria nanoparticles, generally located at the grain boundaries, inhibited the grain corrosion and growth.

Acknowledgments

This investigation was supported by Comunidad de Madrid (S-S2009/MAT-1585), EFDA-ITER (WP13-MAT-W ALLOY), Ministerio de Economía y Competitividad of Spain (ENE2012-39787-C06-05 and MAT2012-38541-c02-02) and CEI Campus Moncloa. The TEM measurements were made at LABMET, TEM Laboratory associated with the Red de Laboratorios de la Comunidad de Madrid.

References

[1] Y. Ueda, H.T. Lee, N. Ohno, S. Kajita, A. Kimura, R. Kasada, T. Nagasaka, Y. Hatano, A. Hasegawa, H. Kurishita, Y. Oya, Phys. Scr. T145 (2011) 014029.
[2] J. Pamela, A. Becoulet, D. Borba, J.-L. Boutard, L. Horton, D. Maisonnier, Fusion Eng. Des. 84 (2009) 194–204.
[3] M. Rieth, J.L. Boutard, et al., J. Nucl. Mater. 417 (2011) 463–467.
[4] P. Norajitra et al., J. Nucl. Mater. 367 (2007) 1416–1421.
[5] P. Norajitra, L.V. Boccaccini, A. Gervash, R. Giniyatulin, N. Holstein, T. Ihli, G. Janeschitz, W. Krauss, R. Kruessmann, V. Kuznetsov, A. Makhankov, I. Mazul, A. Moeslang, I. Ovchinnikov, M. Rieth, B. Zeep, J. Nucl. Mater. 367–370 (2007) 1416–1421.
[6] T. Palacios, J.Y. Pastor, M.V. Aguirre, A. Martin, M.A. Mongue, A. Muñoz, R. Pareja, J. Nucl. Mater. 442 (2013) 277–281.
[7] H. Kurishita, Y. Amano, S. Kobayashi, K. Nakai, H. Arakawa, Y. Hiraoka, T. Takida, K. Takebe, H. Matsui, J. Nucl. Mater. 367–370 (2007) 1453–1457.
[8] I. Wesemann, W. Spielmann, P. Heel, A. Hoffmann, Int. J. Refract. Met. Hard Mater. 28 (2010) 687–691.
[9] J. Martínez, B. Savoini, M.A. Monge, A. Muñoz, R. Pareja, Fusion Eng. Des. 86 (2011) 2534–2537.
[10] M.V. Aguirre, A. Martín, J.Y. Pastor, J. Llorca, M.A. Monge, R. Pareja, J. Nucl. Mater. 404 (2010) 203–209.
[11] A. Muñoz, J. Martínez, M.A. Monge, B. Savoini, R. Pareja, A. Raudulescu, Int. J. Refract. Met. Hard Mater. 33 (2012) 6–9.
[12] W.C. Oliver, G.M. Pharr, J. Mater. Res. 7 (6) (1992).
[13] Standard Test Method for Dynamic Young's Modulus, Shear Modulus, and Poisson's Ratio for Advanced Ceramics by Impulse Excitation of Vibration, ASTM C1259-98, Annual Book of ASTM Standards, American Society for Testing and Materials, West Conshohocken, Pennsylvania, 1999, pp. 386–400 (15.01).
[14] Mark S.M. Alger, Polymer Science Dictionary, Springer, 1997. ISBN 0412608707.
[15] R. Ulick, The Corrosion and Oxidation of Metals, Edward Arnold Ltd., London, 1976.
[16] S. Timoshenko, Strength of Materials, third ed., D. Van Nostrand Company, 1955.
[17] G.V. Guinea, J.Y. Pastor, J. Planas, Int. J. Fract. 89 (2) (1998).
[18] Lyubomira Veleva, Contribution to the Production and Characterization of W–Y, W–Y_2O_3 and W–TiC Materials for Fusion Reactors. Dissertation for the École Polythechnique Féderale de Lausanne, 4995, April 2011.
[19] M.A. Monge, M.A. Auger, T. Leguey, Y. Ortega, L. Bolzoni, E. Gordo, R. Pareja, J. Nucl. Mater. 386–388 (2009) 613–617.
[20] V. Swamy, H.J. Seifert, F. Aldinger, J. Alloys Compd. 269 (1998) 201–207.
[21] H.J. Ryu, S.H. Hong, Mater. Sci. Eng. A363 (2003) 179–184.
[22] M. Battabyal, R. Schäublin, P. Spätig, M. Walter, M. Rieth, N. Baluc, J. Nucl. Mater. 442 (2013) 225–228.
[23] S.C. Cifuentes, M.A. Monge, P. Perez, Corros. Sci. 57 (2012) 114–121.